Lithos 140–141 (2012) 142–151

Contents lists available at SciVerse ScienceDirect

Lithos

journal homepage: www.elsevier.com/locate/lithos

An oxygen fugacity profile through the Siberian Craton — Fe K-edge XANES determinations of $Fe^{3+}/\sum Fe$ in garnets in peridotite xenoliths from the Udachnaya East kimberlite

Gregory M. Yaxley [a,*], Andrew J. Berry [b], Vadim S. Kamenetsky [c], Alan B. Woodland [d], Alexander V. Golovin [e]

[a] Research School of Earth Sciences, The Australian National University, Canberra ACT 0200, Australia
[b] Department of Earth Science and Engineering, Imperial College London, South Kensington Campus, London SW7 2AZ, UK
[c] ARC Centre of Excellence in Ore Deposits, University of Tasmania, Private Bag 126, Hobart Tas 7001, Australia
[d] Institut für Geowissenschaften, Universität Frankfurt, Altenhöferallee 1, 60438 Frankfurt, Germany
[e] Sobolev Institute of Geology and Mineralogy, Novosibirsk, Russia

ARTICLE INFO

Article history:
Received 24 October 2011
Accepted 19 January 2012
Available online 1 February 2012

Keywords:
XANES
Garnet peridotite xenoliths
Siberian Craton
Oxygen fugacity
Metasomatism

ABSTRACT

The Udachnaya East kimberlite sampled garnet peridotite xenoliths from a pressure range of 1.2 to 7.1 GPa in the underlying Siberian cratonic lithosphere. Samples derived from <5.2 GPa lie close to a typical cratonic geotherm of 40 mW m^{-2}, whereas more deeply derived samples have temperatures ≥100 °C above this geotherm. Minor and trace element compositions of garnet and clinopyroxene indicate the presence of both depleted and metasomatically enriched material in the suite. Depleted material derives from the entire sampled depth interval, but enriched material is confined to pressures of 4.5 to 6.6 GPa. Thus, the Siberian cratonic lithosphere under the Undachnaya pipe consisted of a relatively cool and depleted upper layer about 150 km deep, underlain by a hotter layer which extended to at least 210 km depth and contained both depleted and enriched material. Fe K-edge XANES was applied to garnets from this suite to measure their $Fe^{3+}/\sum Fe$ values, enabling determination of a redox profile through the lithospheric section represented by the xenolith suite. $\Delta \log fO_2^{[FMQ]}$ varied from −2.5 to nearly −6.0 over the sampled pressure interval. An overall trend to lower $\Delta \log fO_2^{[FMQ]}$ values with increasing pressure was defined mostly by the depleted samples. A superimposed oxidation trend to $\Delta \log fO_2^{[FMQ]}$ values 1–2 units higher than the main trend mostly affected the deeper, enriched samples, indicating a clear link between metasomatism and oxidation. The amount of oxidation was insufficient to de-stabilize diamond in the deep lithosphere. A possible mechanism for metasomatic enrichment relates to localized, low degree "redox melting", whereby upwardly percolating $CH_4 \pm H_2O$ fluids would encounter progressively more oxidizing peridotite wall-rock resulting in diamond crystallization and increased water activity in the fluid. This could lead to local partial melting and enriched melts could migrate into cooler parts of the lithosphere and crystallize, thus enriching parts of the lithosphere. Melts thus formed are expected to be relatively enriched in Fe^{3+} as it is moderately incompatible during partial melting. Lithospheric domains metasomatised by solidification of these melts would be relatively enriched in Fe^{3+} and garnets may therefore have higher $Fe^{3+}/\sum Fe$ values, thus recording relatively higher $\Delta \log fO_2^{[FMQ]}$ values.

1. Introduction

The oxygen fugacity (fO_2) of the Earth's mantle is an important but often overlooked variable, which controls speciation of fluids in the CHOS system and therefore influences many processes such as partial melting, metasomatism and diamond stability (e.g. Taylor and Green, 1987, 1988). Oxygen fugacity of the deep cratonic mantle is recorded by garnet peridotite xenoliths, which have been accidentally entrained in, and rapidly transported by kimberlite magmas to the uppermost crust or surface, where they are quenched. Their mineral chemistry retains records of pressure (P), temperature (T) and fO_2 in the lithosphere from where they were sampled. fO_2 is recorded by the valence state of multivalent transition metals in the xenoliths' minerals. Fe is the most abundant transition metal in mantle assemblages, existing in both 2+ and 3+ oxidation states. Oxygen fugacity in peridotite is buffered by silicate–oxide exchange equilibria involving the phases in which Fe can exist in multiple oxidation states, spinel, garnet and pyroxenes. In the garnet peridotite facies, the most important reaction is

$$\underset{\text{skiagite}}{2Fe^{2+}{}_3Fe^{3+}{}_2Si_3O_{12}}[\text{garnet}] = \underset{\text{fayalite}}{4Fe_2SiO_4}[\text{olivine}] + \underset{\text{ferrosilite}}{2FeSiO_3}[\text{opx}] + O_2 . \quad (1)$$

* Corresponding author. Tel.: +61 2 6125 8334; fax: +61 2 6125 4835.
E-mail address: greg.yaxley@anu.edu.au (G.M. Yaxley).

0024-4937/$ – see front matter © 2012 Elsevier B.V. All rights reserved.
doi:10.1016/j.lithos.2012.01.016

Thus, garnet in peridotite acts as a redox sensor, recording mantle fO_2 from the garnet skiagite activity, or by the $Fe^{3+}/(Fe^{2+}+Fe^{3+})$ (or $Fe^{3+}/\sum Fe$) value of the garnet (Gudmundsson and Wood, 1995).

Experimental studies and thermodynamic modeling (e.g. Belonoshko and Saxena, 1992; Taylor and Green, 1987; Woodland and Koch, 2003) have shown that CHO-fluids under reduced fO_2 conditions exist predominantly as CH_4+H_2O, with the proportions of each molecular species dependent on fluid composition. According to thermodynamic calculations by Woodland and Koch (2003) a CHO-fluid at $\Delta \log fO_2^{[FMQ]}$ [fO_2 relative to the fayalite–magnetite–quartz redox buffer (Frost, 1991)] of about −5.5 may contain about 75% CH_4 and 25% H_2O at 6 GPa and 1400 °C. If such a reduced fluid encountered progressively more oxidized conditions, it could intersect the carbon-saturation surface (Taylor and Green, 1987) whereupon it would crystallize graphite or diamond (depending on the pressure and temperature conditions) leaving a H_2O-rich residual fluid. In the model of Woodland and Koch (2003) an increase in fO_2 by 3 orders of magnitude will result in oxidation of methane to diamond and almost all carbon will be removed from the fluid, leaving a H_2O-rich fluid. This increase in water activity in the fluid may flux melting of mantle peridotite leading to the process known as "redox melting" (Foley, 2011; Taylor and Green, 1987, 1988).

Mantle fO_2 is also an important variable controlling diamond/graphite stability. In peridotite assemblages, diamond/graphite versus carbonate stability is determined by buffering reactions such as EMOD/G:

$$\underset{\text{enstatite}}{MgSiO_3}+\underset{\text{magnesite}}{MgCO_3}=\underset{\text{olivine}}{Mg_2SiO_4}+C+O_2 \quad (2)$$

in harzburgitic assemblages or by EMFDD:

$$3\underset{\text{enstatite}}{MgSiO_3}+\underset{\text{calcite}}{CaCO_3}=\underset{\text{olivine}}{Mg_2SiO_4}+\underset{\text{diopside}}{CaMgSi_2O_6}+C+O_2 \quad (3)$$

in lherzolitic assemblages (Eggler and Baker, 1982; Luth, 1993). Therefore, direct measurement of the fO_2 recorded by mantle samples may allow constraints to be placed on processes such as diamond crystallization or resorption, partial melting and metasomatism. We report here the first redox measurements from a suite of garnet peridotite xenoliths from the Udachnaya East kimberlite. We have applied the newly developed Fe K-edge XANES technique (Berry et al., 2010) to measure $Fe^{3+}/\sum Fe$ in garnets from the suite. This technique has advantages over Mössbauer spectroscopy and the flank method, relating to superior spatial resolution and significantly shorter data acquisition times (Berry et al., 2008; Berry et al., 2010), but can determine garnet $Fe^{3+}/\sum Fe$ with similar precision (±0.01). In conjunction with conventional thermobarometry and trace element measurements in garnet and clinopyroxene using LA-ICPMS, we establish (1) a redox profile over a depth interval from ≈90 to ≈220 km in the Siberian Craton of decreasing $\Delta \log fO_2^{[FMQ]}$ with increasing depth, and (2) a superimposed oxidation clearly associated with metasomatism at depths greater than ≈130 km. We also show that all samples, including those oxidized by metasomatism, lie in the diamond/graphite stability field, at least 1.0–1.5 units below the EMOD/G buffering reaction in depth-fO_2 space.

2. Geological setting and nature of the samples

The Udachnaya kimberlite is one of >1100 kimberlite bodies in Yakutia in the Russian Federation (Ashchepkov et al., 2010). It was emplaced into the central Siberian Craton 367 Ma ago (Kinny et al., 1997). The kimberlite consists of two branches of a main pipe, the eastern (Vostok) and the western. The current samples were derived from depths of 400–480 m or more below the surface, in the eastern pipe, where recent mining operations have recovered very fresh peridotite xenoliths. Detailed petrographic, mineralogical and geochemical studies of other fresh garnet peridotite xenoliths from Udachnaya East kimberlite pipe were recently reported by Ionov et al. (2010) and Agashev et al. (2010).

The current 21 samples are small fragments of larger xenoliths. Our samples are typically a few centimeters across. They are generally very fresh with only minor or no visible serpentinization of olivines and minor development of kelyphitic breakdown rims on garnets. All samples are garnet peridotites and clinopyroxene was observed in 18 of them. The small size of most samples in this study makes it difficult to estimate reliable phase proportions. Texturally, the samples vary from coarse granular textures (e.g. Uv28/05, Uv129/03, Uv101/03) to porphyroclastic (which exhibit minor recrystallisation of olivine to fine-grained neoblasts along porphyroblastic olivine margins — e.g. Uv67/03, Uv101/03) to sheared samples in which coarse euhedral garnets and coarse pyroxenes are set in very fine-grained, sheared matrix of olivine crystals (e.g. Uv68/03).

3. Analytical methods

Major and minor element compositions of constituent phases in the xenoliths were determined by WDS electronprobe microanalysis using the Cameca SX-100 in the Central Science Laboratory, University of Tasmania. The accelerating voltage was 15 kV and the beam current was 20 nA. The beam diameter was focused to 1 μm. Elemental calibration was performed on a range of well-characterized natural mineral standards.

Trace element compositions of garnet and clinopyroxene from 16 of the 21 samples were determined by LA-ICPMS using the Agilent 7500 instrument at The Australian National University. Analytical protocols were similar to those reported in Eggins et al. (1998).

The Fe^{3+} content of garnet was determined for 14 of the 21 samples using the Fe K-edge XANES technique recently described by Berry et al. (2010). This technique depends on the establishment of an empirical calibration curve, which relates the ratio of the intensity of post-edge features at 7138.4 and 7161.7 eV in the Fe K-edge XANES spectra of a series of standard garnets to their $Fe^{3+}/\sum Fe$ value previously determined by Mössbauer spectroscopy. Berry et al. (2010) noted that the normalized intensity ratio of these features correlated with $Fe^{3+}/\sum Fe$ for a suite of standard garnets which cover most of the compositional range exhibited by garnets from garnet peridotite xenoliths hosted by kimberlites.

The standard garnets were from garnet peridotite xenoliths from Diavik kimberlite (Slave Craton, Canada) (Yaxley, *unpublished data*) and from the several kimberlite localities in the Kaapvaal Craton (Kimberley, Jagersfontein, Frank Smith Mine and Monastery in South Africa and Letseng-la-Terae, Liqhobong and Matsoku in Lesotho) (Woodland and Koch, 2003). These samples have $Fe^{3+}/\sum Fe$ ranging from 0.034 to 0.134 as established by Mössbauer spectroscopy. A correction for recoil-free fractions in the Mössbauer spectra was made following the derivation of Woodland and Ross (1994). Woodland et al. (2009) demonstrated that this correction is also valid for Cr-bearing garnets such as the standard garnets used here.

The Fe K-edge XANES spectra were recorded at the X-ray Fluorescence Microscopy (XFM) beamline (Paterson et al., 2011) of the Australian Synchrotron. The excitation energy was selected using a Si(111) double crystal monochromator. The energy was calibrated for each sample by simultaneously recording an Fe foil spectrum using light scattered by a sheet of plastic (2 mm thick) inserted in the beam path (upstream of the normalization ion chamber used for the microprobe) and a foil mounted in front of a photodiode (e.g. Cross and Frenkel, 1999). The first derivative of this Fe spectrum was defined to be 7112.0 eV. The beamline spectral resolution was 1.9 eV. The spatial resolution was defined by KB mirrors, which produced an analysis spot of ~3×3 μm for this study. Samples were mounted at 45° to both the incident beam and a single element silicon drift energy dispersive detector (Vortex EM, SII Nanotechnology, Northridge, CA) with digital signal processing (DXP Saturn, XIA LLC,

Hayward, CA). All spectra were recorded in fluorescence mode and the incident flux and sample-detector distance were adjusted to ensure that the total incoming count rate was within the linear range of the detector. Spectra were recorded from 7075 to 7300 eV and compared after subtraction of a constant baseline and normalization to the average intensity above 7235 eV. Representative spectra are shown in Fig. 1 and the calibration curve, which is the linear best fit to the data obtained from the standards, is shown in Fig. 2. The uncertainty in the $Fe^{3+}/\sum Fe$ values of the standards is estimated to be ± 0.01. The standard deviation of the difference between the $Fe^{3+}/\sum Fe$ values of the standards and the line of best fit is ± 0.008. This suggests that the uncertainty in values obtained using the calibration curve is not larger than that of the Mössbauer data and hence we estimate the accuracy of our results to be ± 0.01. The $Fe^{3+}/\sum Fe$ values determined for the Udachnaya samples using this calibration curve are given in Table 2.

4. Mineral chemistry

Average major, minor and trace element mineral compositions from some representative samples are presented in Table 1, and the full data set is presented in the Supplementary Data.

Olivine grains range in Mg# from 89.6 to 92.3 [where $Mg\# = 100\ Mg/(Mg + Fe^{2+})$], in MnO content from 0.10 to 0.16 wt.% and NiO content from 0.38 to 0.45 wt.%. Mg# and MnO are negatively correlated. As was observed by Ionov et al. (2010), there is a tendency for the sheared xenoliths from Udachnaya to have olivines with Mg#s at the lower end of the Mg# range. Overall, the olivine compositions of the current suite are very similar to those reported in earlier studies of Udachnaya garnet peridotite xenoliths (Boyd et al., 1997; Ionov et al., 2010; Sobolev et al., 2009).

Orthopyroxene grains vary in Al_2O_3 content from 0.35 to 0.90 wt.% (excluding sample Uv101/03 in which orthopyroxene contains 3.54 wt.% Al_2O_3) and 0.27 to 1.22 wt.% CaO. Cr_2O_3 contents range from 0.20 to 0.50 wt.% and TiO_2 is $\leq$0.17 wt.%. Uv101/03 may be spinel-bearing, based on its aluminous pyroxene composition, although spinel was not observed petrographically in this sample. This is also consistent with its much lower P-T estimates from thermobarometry (1.2 GPa, 723 °C — see Section 5.1.

Garnet grains are un-zoned in all measured major and minor elements, except for sample Uv89/03 in which TiO_2 content on the rims of the grains is higher (1.08 wt.%) than in the cores (0.59 wt.%). This sample exhibits a sheared texture and similar Ti-zoning in garnets was reported by Ionov et al. (2010), Shimizu et al. (1997) and Boyd et al. (1997). Garnet Mg#s vary from 80.4 to 84.8. As with olivine,

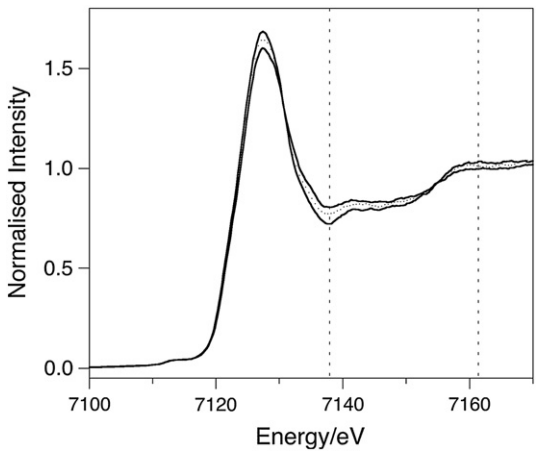

Fig. 1. Fe K-edge XANES spectra of Udachnaya samples Uv9/05 ($Fe^{3+}/\sum Fe = 0.031$), Uv87/03 ($Fe^{3+}/\sum Fe = 0.132$) (solid lines) and Diavik standard 507111505 ($Fe^{3+}/\sum Fe = 0.099$) (dotted line). The dashed lines correspond to 7138.4 and 7161.7 eV.

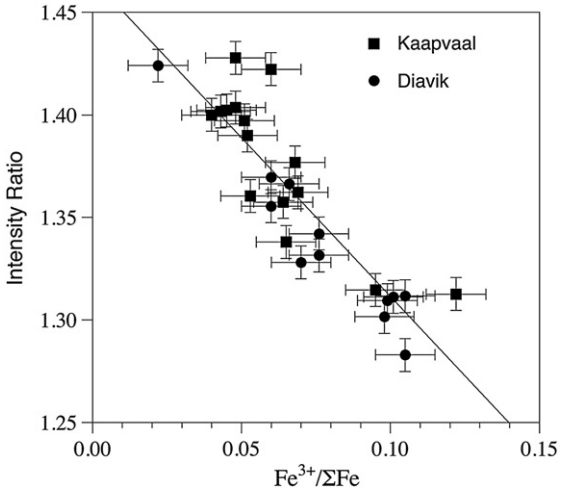

Fig. 2. Calibration curve (line of best fit) relating the intensity ratio of features at 7138.4 and 7161.7 eV in the XANES spectrum with $Fe^{3+}/\sum Fe$ determined by Mössbauer spectroscopy for garnets from the Kaapvaal craton and Diavik kimberlite.

there is a tendency for the sheared xenoliths to have garnet Mg#s at the lower end of the range. Garnet $Fe^{3+}/\sum Fe$ determined by XANES varies from 0.026 to 0.14, a range of values fairly typical of Cr-pyrope garnets from cratonic lithosphere (e.g. Creighton et al., 2009; Creighton et al., 2010; Woodland and Koch, 2003). CaO varies from 4.34 to 6.89 wt.% and correlates positively with Cr_2O_3 contents (2.81 to 9.21 wt.%) ($r^2 = 0.85$) (Fig. 3). Using the garnet classification scheme of Grütter et al. (2004), which is largely based on Ca-Cr systematics, all garnets are G9 (lherzolitic) except those from sample Uv68/03, which are G5 (pyroxenitic). The "pyroxenitic" garnets have the lowest CaO and Cr_2O_3 contents from this suite. For some samples, the garnet classification does not reflect the observed mineralogy, in that clinopyroxene was not detected in three samples containing "lherzolitic" garnet (Uv48/03, Uv67/03, Uv126/03) and because sample Uv68/03 is not pyroxenitic but peridotitic.

Garnet Ti contents exhibit a distinctively bimodal distribution. Six of the 16 samples measured by LA-ICPMS contain <350 ppm Ti, whereas the remainder contain from 900 to 8550 ppm Ti. Ti content also correlates positively with Na, P, Ga, Y and Zr abundances. Systematics amongst Ti, Y and Zr were used by Griffin and Ryan (1995) as an indicator of depletion versus enrichment in Cr-pyrope garnets. Depleted samples contain low abundances (<1000 ppm Ti, <20 ppm Zr, <10 ppm Hf), whereas samples enriched by metasomatic processes contain higher abundances. For the current suite [as well as the suite of Ionov et al. (2010)], Ti–Y and Ti–Zr contents in garnet (and clinopyroxene) are positively correlated, and the suite contains several samples classified as depleted and others classified as metasomatised (Fig. 4).

Garnet REE patterns vary significantly from "strongly sinusoidal" (e.g. Uv45/03 and Uv87/03) to "weakly sinusoidal" (e.g. Uv04/05 and Uv34/03) to "normal" (e.g. Uv100/03 and Uv05/04) (Fig. 5). On Primitive Mantle normalized REE plots (denoted REE_N; Sun and McDonough, 1989), strongly sinusoidal patterns exhibit steeply positively sloping $HREE_N$ segments from Lu to a normalized abundance minimum at either Gd, Tb, Dy or Ho. From the minimum the patterns slope negatively to a normalized abundance maximum at either Pr, Nd or Sm, and then slope negatively to low $LREE_N$ abundances. These garnets are depleted in terms of their Ti, Y and Zr contents. Garnets with weakly sinusoidal patterns or normal patterns exhibit $HREE_N$ to $MREE_N$ segments, which are slightly positively or slightly negatively sloped on the normalized REE diagram. From the MREE to LREE the slope is positive and gradually becomes steeper towards La. In garnets with weakly sinusoidal or normal REE_N patterns, the normalized abundances of HREE and MREE are higher than those in

Table 1
Representative major, minor and trace element data for garnet (ga) and clinopyroxene (cpx) from 5 samples from the suite. Cations were calculated on the basis of 6 oxygen atoms for cpx and 12 for garnet. Garnet Fe^{3+} was measured by Fe K-edge XANES. For cpx, all Fe is assumed to be Fe^{2+}. [Mg# = 100*Mg/(Mg + Fe^{2+})]. "nd" = not determined.

	Uv9-05 cpx	Uv9-05 ga	Uv129-03 cpx	Uv129-03 ga	Uv88-03 cpx	Uv88-03 ga	Uv130-03 cpx	Uv130-03 ga	Uv42-03 cpx	Uv42-03 ga
SiO_2	54.05	40.98	54.33	41.17	55.04	40.73	54.27	41.21	54.68	41.10
TiO_2	0.02	0.03	0.30	0.92	0.00	0.05	0.34	0.05	0.00	0.00
Al_2O_3	1.84	19.84	1.51	19.68	0.48	16.58	1.76	20.60	1.96	21.47
Cr_2O_3	1.76	5.74	1.13	4.05	0.41	8.50	1.40	5.29	1.54	4.24
Fe_2O_3	nd	0.28	nd	0.97	nd	1.05	nd	0.29	nd	0.22
FeO	1.61	7.97	3.41	7.04	2.85	6.20	3.56	7.65	1.47	7.32
MnO	0.11	0.54	0.14	0.34	0.11	0.36	0.13	0.49	0.09	0.47
MgO	16.62	18.68	17.91	20.95	20.71	19.60	18.44	19.80	17.21	19.83
NiO	0.03	0.00	0.05	0.01	nd	0.02	0.06	0.00	nd	0.01
CaO	21.75	6.34	18.91	5.16	19.73	6.78	17.87	5.63	21.49	5.96
Na_2O	1.48	0.03	1.49	0.09	0.14	0.01	1.64	0.02	1.24	0.01
K_2O	0.06	0.01	0.04	0.01	nd	0.00	0.04	0.00	nd	0.00
P_2O_5	0.02	0.01	0.01	0.03	nd	0.01	0.01	0.01	nd	0.00
Total	99.35	100.45	99.23	100.41	99.47	99.90	99.54	101.04	99.68	100.61
Si	1.9710	2.9632	1.9806	2.9543	1.9889	2.9831	1.9704	2.9462	1.9783	2.9386
Ti	0.0006	0.0014	0.0082	0.0494	0.0001	0.0029	0.0093	0.0028	0.0000	0.000
Al	0.0792	1.6913	0.0649	1.6647	0.0206	1.4313	0.0755	1.7365	0.0835	1.8096
Cr	0.0508	0.3282	0.0327	0.2300	0.0116	0.4924	0.0402	0.2993	0.0442	0.2394
Fe^{3+}		0.0155		0.0524		0.0577		0.0157		0.0117
Fe^{2+}	0.0492	0.4837	0.1039	0.4285	0.0862	0.3860	0.1080	0.4590	0.0444	0.4391
Mn	0.0035	0.0331	0.0044	0.0206	0.0035	0.0226	0.0040	0.0299	0.0027	0.0283
Mg	0.9033	2.0129	0.9729	2.2410	1.1154	2.1399	0.9980	2.1097	0.9282	2.1131
Ni	0.0010	0.0003	0.0015	0.005	0.0000	0.0014	0.0019	0.0000	0.0000	0.0005
Ca	0.8498	0.4916	0.7392	0.3964	0.7639	0.5323	0.6954	0.4314	0.8330	04563
Na	0.1044	0.0045	0.1053	0.0126	0.0095	0.0016	0.1155	0.0030	0.0871	0.0008
K	0.0027	0.0007	0.0018	0.0007	0.0000	0.0004	0.0018	0.0002	0.0000	0.0001
P	0.0006	0.0007	0.0002	0.0019	0.0000	0.0007	0.0004	0.0005	0.0000	0.0002
Total	4.0160	8.0272	4.0156	8.0528	3.9997	8.0521	4.0205	8.0342	4.0014	8.0374
Mg#	94.84	80.62	90.35	83.95	92.82	84.72	90.24	82.13	95.43	82.80
P	nd	45	nd	151	nd	82	nd	58	nd	25
Sc	12.9	154	13.6	114	3.23	160	11.4	124	11.4	153
Ti	126	174	1797	5339	19	302	2031	301		22
V	157	205	198	320	61	502	239	303	135	135
Co	17.8	37.1	30.4	44.2	30.9	40.9	21.1	41.2	16.3	38.1
Ni	274	16.1	524	97.8	578	102	395	31.2	257	22.8
Ga	nd	2.60	nd	10.88	nd	6.44	nd	4.50	nd	2.19
Rb	0.07	bd1	0.02	bd1	0.06	bd1	0.51	bd1	0.01	bd1
Sr	25.0	0.12	127	0.56	142	0.98	92.9	0.10	2.38	0.02
Y	0.07	2.28	2.01	18.9	0.02	0.79	0.04	0.95	0.03	1.25
Zr	0.12	1.21	4.86	65.1	0.02	7.29	0.28	1.88	0.04	0.55
Nb	0.03	0.29	0.23	0.53	0.15	2.17	0.12	0.31	0.01	0.20
Ba	11.4	bd1	0.43	bd1	0.87	bd1	129	bd1	1.34	0.11
La	0.94	0.01	2.43	0.05	1.15	0.21	9.31	0.10	0.12	0.003
Ce	1.96	0.05	8.97	0.49	3.74	1.78	11.67	0.48	0.25	0.02
Pr	nd	0.03	nd	0.19	nd	0.50	nd	0.08	nd	0.006
Nd	0.84	0.29	6.93	1.73	1.60	3.15	1.98	0.43	0.06	0.02
Sm	0.07	0.13	1.56	1.36	0.13	0.72	0.15	0.15	0.006	bd1
Eu	0.01	0.05	0.440	0.60	0.03	0.19	0.03	0.05	0.00	bd1
Gd	0.04	0.14	1.15	2.39	0.03	0.43	0.06	0.15	0.00	bd1
Tb	nd	0.03	nd	0.44	nd	0.03	nd	0.02	nd	0.00
Dy	0.02	0.28	0.59	3.28	0.005	0.17	0.01	0.13	0.00	0.07
Ho	nd	0.07	nd	0.66	nd	0.03	nd	0.13	nd	0.04
Er	0.01	0.32	0.17	1.95	0.005	0.11	0.01	0.31	0.00	0.25
Tm	nd	0.06	nd	0.28	nd	0.03	nd	0.03	nd	0.07
Yb	0.004	0.60	0.10	1.99	0.002	0.32	0.00	0.32	0.01	0.76
Lu	0.001	0.12	0.01	0.32	0.001	0.08	0.00	0.07	0.001	0.18
Hf	0.01	0.04	0.29	1.59	0.002	0.14	0.01	0.02	0.003	bd1
Ta	0.01	bd1	0.02	0.04	0.01	0.18	0.03	bd1	0.01	0.00
Pb	0.32	0.55	0.18	0.06	0.27	0.01	1.55	0.02	0.04	0.02
Th	0.01	bd1	0.03	0.02	0.01	0.08	0.22	0.05	0.00	bd1
U	nd	bd1	nd	0.02	nd	0.08	nd	0.01	nd	bd1

garnets with strongly sinusoidal patterns. The garnets with weakly sinusoidal or normal REE_N patterns are also relatively enriched in terms of their Ti, Y and Zr contents.

Clinopyroxenes vary in CaO content from 16.60 to 23.75 wt.%, in Na_2O from 0.05 to 1.89 wt.% and in Cr_2O_3 from 0.21 to 2.01 wt.%. Mg^* ranges from 89.3 to 95.6 [where $Mg^* = 100\ Mg/(Mg + Fe_{total})$]. Ti abundance is bi-modal, with 6 samples having $\leq$0.05 wt.% TiO_2 and the remainder having $\geq$0.15 wt.%. Most samples with Ti-depleted garnets have Ti-depleted clinopyroxene. Clinopyroxene normalized REE patterns exhibit two distinct broad types, which we designate here "sinusoidal", and "normal" patterns (Fig. 6). Sample Uv101/03 exhibits an unusual sinusoidal pattern in which the HREE

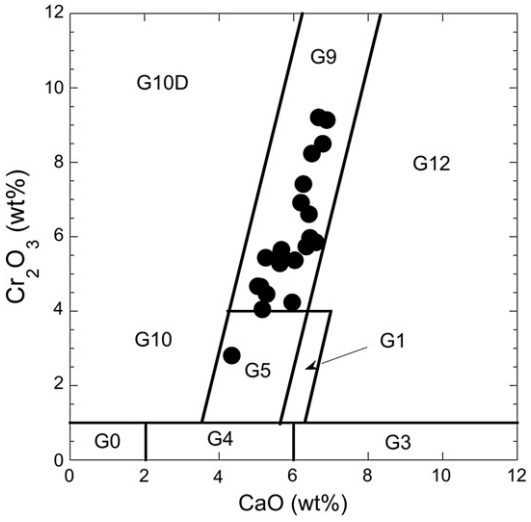

Fig. 3. Classification of garnets from this suite (Grütter et al., 2004), based on CaO–Cr_2O_3 systematics.

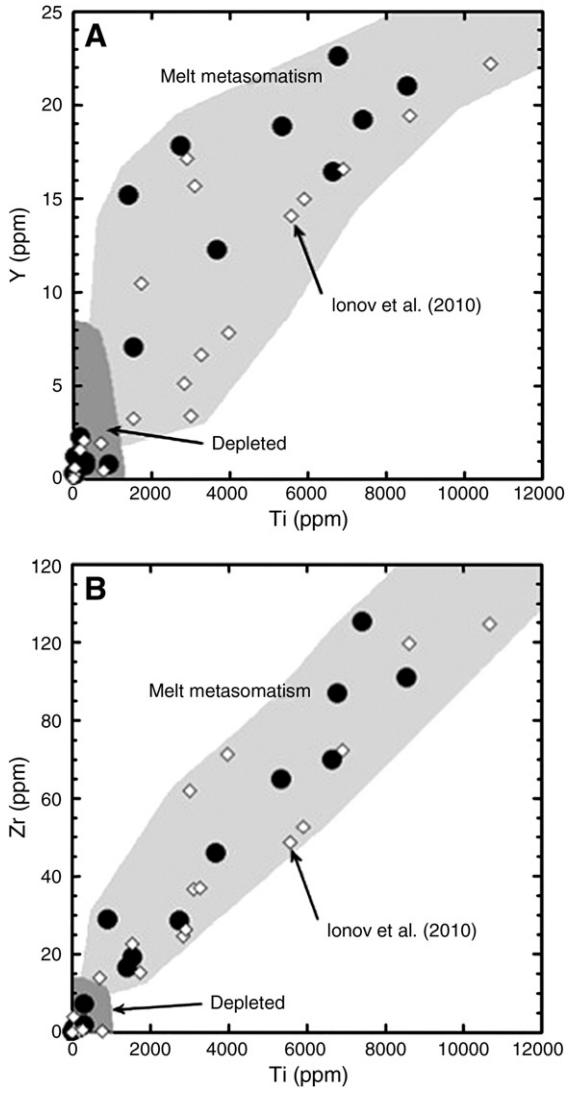

Fig. 4. Plots of Y (A) and Zr (B) contents against Ti contents in garnets from the current samples (black circles) and the Udachnaya samples of Ionov et al. (2010) (open diamonds). "Depleted" and "Melt metasomatism" fields are after Griffin and Ryan (1995).

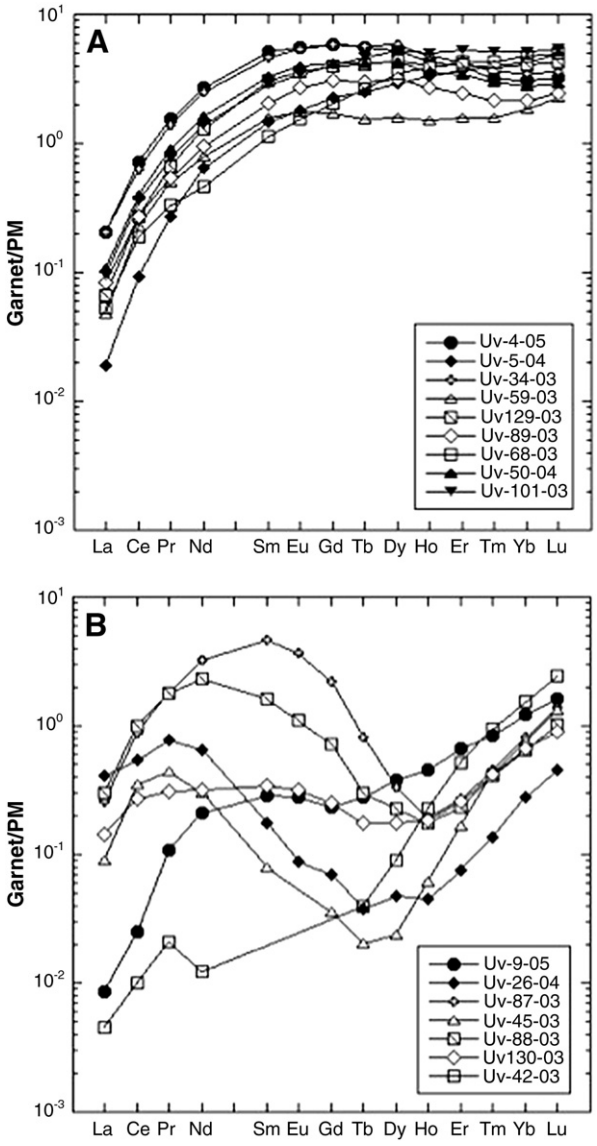

Fig. 5. Primitive Mantle normalized (Sun and McDonough, 1989) REE plots of garnets from the current suite. (A) Garnets with normal to weakly sinusoidal patterns; (B) garnets with strongly sinusoidal patterns.

segment is positively sloped from Lu to a normalized abundance minimum at Ho. From Ho to Nd the pattern is gently negatively sloped, but slopes positively from a maximum at Nd down to La. Sinusoidal patterns from other samples (samples Uv09/05, Uv26/04, Uv87/03, Uv45/03, Uv88/03, Uv130/03 and Uv101/03) are positively sloped from Lu to Yb, and then smoothly and negatively sloped from Yb to a maximum at Ce or La. Collectively, they exhibit only a small variation in HREE abundances, but normalized M-LREE abundances vary over several orders of magnitude. This contrasts with the "normal" group (Uv50/04, Uv4/05, Uv34/03, Uv59/03, Uv129/03, Uv89/03 and Uv68/03), in which the patterns are smooth and negatively sloped to a maximum at Ce, and positively sloped from Ce to La. REE abundances overall are similar in clinopyroxene with "normal" patterns from different samples.

Except for Uv50/04, clinopyroxenes with "normal" REE_N patterns come from samples in which garnets are enriched in Ti, Zr and Y and exhibit weakly sinusoidal to normal REE_N patterns (Kamenetsky et al., 2009). Conversely, clinopyroxenes with "sinusoidal" REE_N patterns come from samples in which garnets are depleted in Ti, Zr and Y and exhibit strongly sinusoidal REE_N patterns (Figs. 5 and 6).

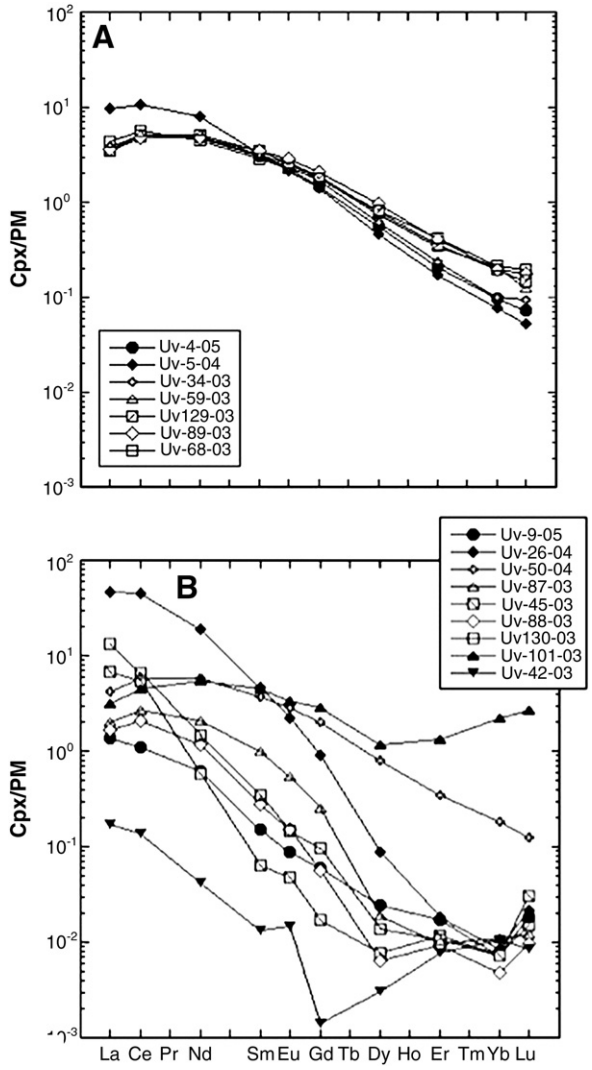

Fig. 6. Primitive Mantle normalized (Sun and McDonough, 1989) REE plots of clinopyroxenes from the current suite. (A) Clinopyroxenes with normal patterns; (B) clinopyroxenes with sinusoidal patterns.

Table 2
Results of thermobarometric and redox calculations. P[NG85] and T[TA98] are pressure and temperature of equilibration of the xenoliths following the method of Nimis and Grütter (2010). $Fe^{3+}/\sum Fe$ values were determined using the Fe K-edge XANES technique described by Berry et al. (2010) and $\Delta \log fO_2^{[FMQ]}$ was calculated using the calibration of Gudmundsson and Wood (1995). $\Delta \log fO_2^{[FMQ]*}$ was calculated for samples with P[NG85] > 4 GPa, incorporating the phase compressibility data from Woodland et al. (1999).

	P[NG85] GPa	T[TA98] (°C)	$Fe^{3+}/\sum Fe$	$\Delta \log fO_2^{[FMQ]}$	$\Delta \log fO_2^{[FMQ]*}$
Uv-4-05	6.23	1292	0.115	−3.7	−3.4
Uv-5-04	4.54	895			
Uv-9-05	3.10	770	0.031	−2.5	
Uv-26-04	5.16	962	0.079	−3.4	−3.1
Uv-50-04	5.61	1278	0.037	−5.0	−4.7
Uv129-03	5.35	1168	0.109	−3.3	−3.1
Uv-87-03	6.12	1324	0.132	−3.6	−3.3
Uv-59-03	5.93	1244	0.085	−4.0	−3.7
Uv-45-03	3.70	899	0.038	−3.0	
Uv-88-03	6.90	1364	0.13	−4.0	−3.7
Uv130-03	7.06	1259	0.033	−5.9	−5.6
Uv-101-03	1.18	723			
Uv-68-03	5.27	1234	0.086	−3.6	−3.2
Uv-89-03	6.44	1253	0.089	−4.3	−4.0
Uv-34-03	6.13	1290	0.139	−3.4	−3.1
Uv-42-03	3.88	947	0.026	−4.0	
Uv-37-03	4.53	851			
Uv-28-05	3.48	854			

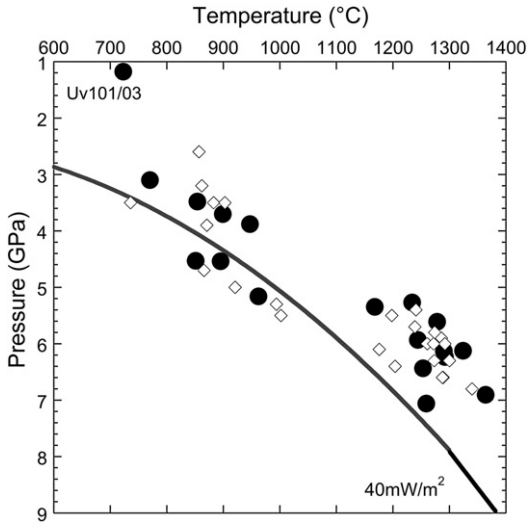

Fig. 7. Plot of P[NG85] against T[TA98] (Nimis and Grütter, 2010) for the current suite (black circles) and the Udachnaya garnet peridotites described by Ionov et al. (2010). The curved line is an estimated 40 mW m^{-2} geotherm (Pollack and Chapman, 1977).

5. Discussion

5.1. Thermobarometry

Several thermometers and barometers previously calibrated with data from high-pressure experiments and from natural samples were used to calculate pressures and temperatures of equilibration of the xenoliths using the approach of Nimis and Grütter (2010). This calculates temperature (T[TA98]) based on an empirical correction by Taylor (1998) to the Brey and Kohler (1990) Ca-in-opx thermometer (T[BKN]), using for input pressure the Al-in-orthopyroxene barometer of Nickel and Green (1985) (P[NG85]). T[TA98] varied from 723 to 1364 °C. P[NG85] varied from 1.18 to 7.06 GPa. Thermobarometric results are presented in Table 2.

The samples exhibit a distribution in P-T space broadly consistent with a cratonic geotherm (Fig. 7). An exception is Uv101/03 which returned P[NG85]-T[TA98] estimates of 1.18 GPa and 723 °C, that are well off any feasible geotherm. The remaining samples exhibit a bimodal temperature distribution, with approximately half the samples recording T[TA98] < 1000 °C at P[NG85] < 5.2 GPa and the other half recording T[TA98] > 1150 °C at P[NG85] > 5.2 GPa. Thus, the temperature interval between 1000 and 1150 °C is not represented in this suite, although the pressure varies continuously from 3.10 to 7.06 GPa. The lower temperature and lower pressure group of samples (except Uv101/03) cluster around an estimated cratonic geotherm with heat flow of ≈40 mW m^{-2} (Pollack and Chapman, 1977), while the high temperature and high pressure group lie at temperatures mostly ≥100 °C above than this geotherm. In agreement with another recent study of a suite of Udachnaya garnet peridotite xenoliths (Ionov et al., 2010), most of the current high temperature samples exhibit sheared textures.

5.2. Metasomatism

Evidence for metasomatism of some of the samples from this suite relates to the range of Ti, Y and Zr in garnet and co-existing clinopyroxene, and the REE_N patterns in garnet and clinopyroxene (Stachel et al., 1998, 2004). Some samples are clearly relatively depleted with garnet Ti < 1000 ppm, Zr < 20 ppm and Hf < 10 ppm, but most are enriched, containing garnets with significantly higher abundances of these three elements (Griffin and Ryan, 1995). Furthermore, samples with low-Ti garnets have strongly sinusoidal garnet REE_N patterns and sinusoidal clinopyroxene REE_N patterns. Samples that contain Ti-rich garnets

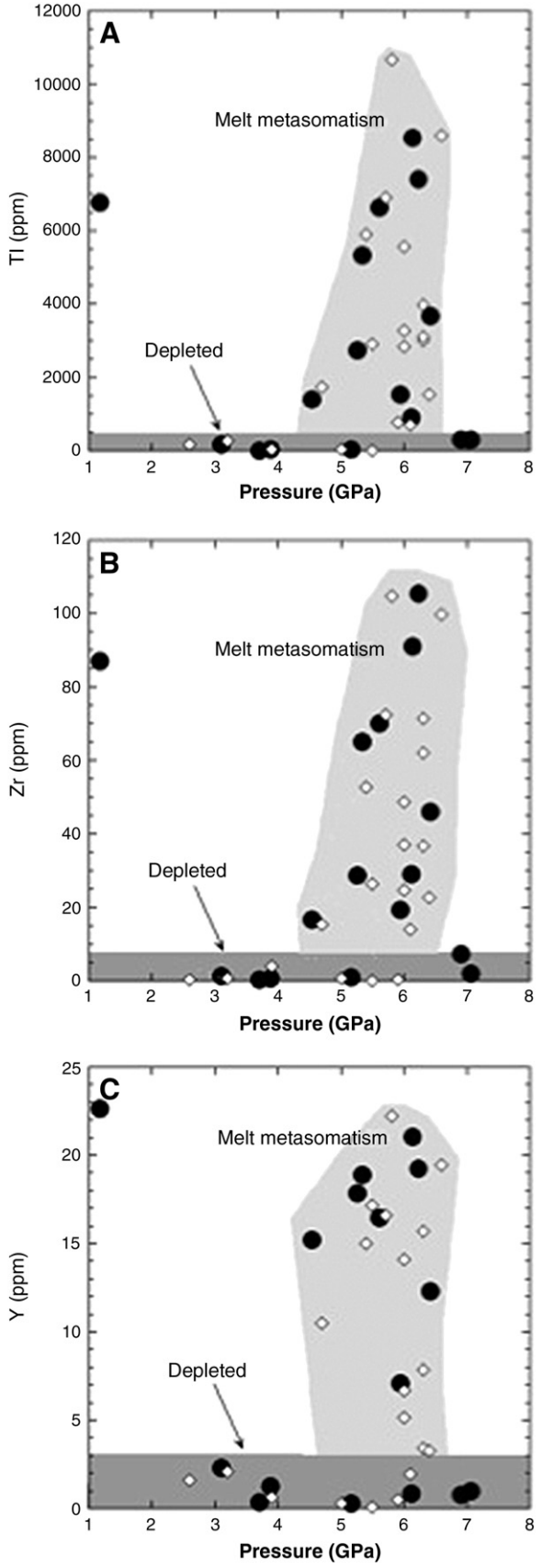

Fig. 8. Plot of (A) garnet Ti content (B) garnet Zr content and (C) garnet Y content against P[NG85], showing the presence of depleted material from the entire sampled depth range and enriched material from a restricted depth interval (4.5–6.6 GPa). "Depleted" and "Melt metasomatism" fields are after Griffin and Ryan (1995). Symbols as in Fig. 3.

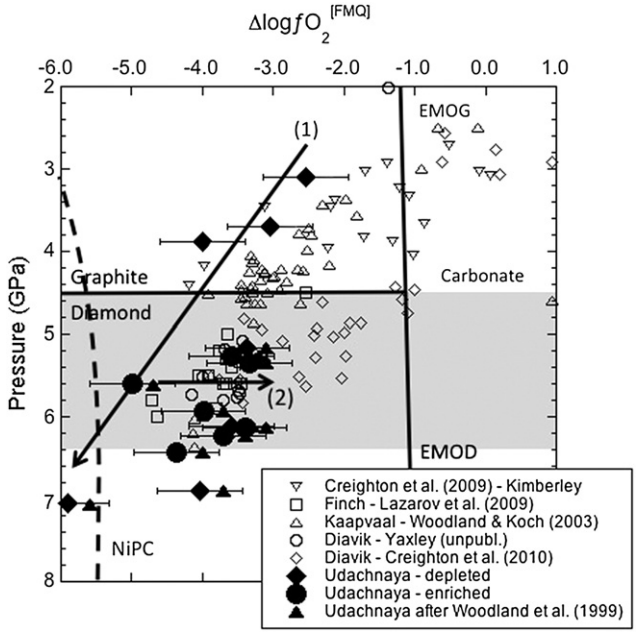

Fig. 9. Plot of $\Delta\log fO_2^{[FMQ]}$ versus equilibration pressure for the current depleted (black diamonds) and enriched samples (black circles), and other samples from various locations in the Kaapvaal Craton and from the Diavik Diamond Mine. The Udachnaya samples have error bars for $\Delta\log fO_2^{[FMQ]}$ of ±0.6 units. Also shown for the Udachnaya samples with P[NG85] > 4 GPa, is $\Delta\log fO_2^{[FMQ]*}$ (black triangles), calculated allowing for the compressibilities of skiagite and other relevant garnet end-members, ferrosilite and fayalite (Woodland et al., 1999). The gray arrow labeled (1) is interpreted as the main trend of decreasing oxygen fugacity with increasing pressure (depth) in the Siberian Craton and is mainly exhibited by depleted samples. The gray arrow labeled (2) represents an oxidation trend associated with metasomatic enrichment. The gray shaded field represents the depth interval in which most Udachnaya samples were enriched, from Fig. 8. The pressure of the graphite/diamond transition is based on a 40 mW m^{-2} geotherm. EMOG and EMOD refer to the diamond limiting reaction enstatite + magnesite = olivine + C + O_2 (Luth, 1993) in the graphite and diamond stability fields respectively. NiPC is the Ni precipitation curve from O'Neill and Wall (1987).

have normal to weakly sinusoidal garnet REE_N patterns and normal clinopyroxene REE_N patterns.

When these indicators of depletion or metasomatism are compared with the depth of origin of the xenoliths, it is apparent that all enriched or metasomatised samples derived from a relatively restricted pressure interval of 4.5–6.6 GPa, whereas depleted samples were derived from the entire sampled depth interval of 2.6–7.1 GPa (Fig. 8). This suggests a vertical lithospheric section under Udachnaya 367 Ma ago, in which a depleted layer, shallower than about 130 km, was underlain by a variably enriched to depleted zone which extends to at least 180 km depth. A similar structure for the Siberian Craton was suggested by Pokhilenko et al. (1999).

5.3. An oxygen fugacity profile in the Siberian Craton

Oxygen fugacities (fO_2) for the samples were calculated using the experimental calibration of Gudmundsson and Wood (1995) for the fO_2 buffering reaction (1) for garnet peridotite assemblages. T [TA98], P[NG85] and the XANES-determined $Fe^{3+}/\sum Fe$ values for garnet were used in the calculations. Results are expressed relative to the fO_2 of the FMQ buffer ($\Delta\log fO_2^{[FMQ]}$) at the P-T conditions of each sample, in the usual fashion, in Table 2. $\Delta\log fO_2^{[FMQ]}$ varies from −5.9 to −2.5. The uncertainty resulting from the uncertainty of the XANES measurements (±0.01 in $Fe^{3+}/\sum Fe$) and in the oxybarometer's calibration is estimated to be ±0.6 (Gudmundsson and Wood, 1995).

Because of the large lithospheric depth interval and the range from relatively depleted to enriched, represented by these xenoliths,

this data allows the fO_2 variation in the Siberian Craton to be profiled as functions of pressure and effects of metasomatism. When $\Delta\log fO_2^{[FMQ]}$ is plotted against P[NG85] an overall trend to lower $\Delta\log fO_2^{[FMQ]}$ with increasing pressure is defined by five samples (Uv09/05, Uv45/03, Uv42/03, Uv50/04, Uv130/03), and of those, four are depleted based on their garnet and clinopyroxene chemistry (Fig. 9). This trend most likely reflects the positive molar volume change of the fO_2 buffering reaction for garnet peridotite assemblages (reaction 1), which forces a shift to higher skiagite activities and to lower fO_2 with increasing pressure (Frost and McCammon, 2008; Woodland and Koch, 2003). Superimposed on this is an oxidation trend, resulting in an increase in $\Delta\log fO_2^{[FMQ]}$ by approximately 1–2 units and which is almost completely restricted to samples from the enriched pressure interval of 4.5 to 6.6 GPa. Seven of the nine samples in the oxidized zone have enriched garnet and clinopyroxene chemistry indicative of metasomatism. The two remaining samples are not enriched in their mineral chemistry but are apparently still oxidized, relative to the main P-$\Delta\log fO_2^{[FMQ]}$ trend.

Fig. 9 also illustrates the Ni precipitation curve (NiPC; Frost and McCammon, 2008; O'Neill and Wall 1987) along a 40 mW m^{-2} geotherm (Pollack and Chapman, 1977). Two of the samples (Uv130/03 and Uv50/04) apparently plot below this curve and therefore should contain (or have contained) a metallic FeNi alloy. Segregation of such a molten alloy would have depleted the residual silicate components in Fe and Ni, but there is no evidence in their mineral chemistry that this occurred. The most likely explanation relates to uncertainties in the Gudmundsson and Wood (1995) oxybarometer employed in the calculations. The quoted uncertainty in this oxybarometer is ±0.6 log units, meaning that sample Uv50/04 (5.6 GPa) is within error of the NiPC on Fig. 9. This is not the case for sample Uv130/03 (7.1 GPa). However, Woodland et al. (1999) pointed out that the pressure effect described above becomes less at high pressures when the compressibilities of skiagite and other garnet endmembers, as well as fayalite and ferrosilite, are taken into account in the calculations. When this is done for samples equilibrated at 6–7 GPa, fO_2 values increase by 0.3–0.5 log units (Woodland et al., 1999). Table 1 and Fig. 9 also include recalculated fO_2 values for the high pressure samples incorporating this correction for the phase compressibilities (Woodland et al., 1999). In the case of Uv130/03 (the 7.1 GPa sample) this will place it well within error of the NiPC curve (Fig. 9). Accounting for this effect shifts the $\Delta\log fO_2^{[FMQ]}$s of all high pressure samples from this suite (i.e. those at 6–7 GPa) to somewhat higher values but does not alter the major conclusions of this paper. However, we believe it appropriate to base our discussion on the $\Delta\log fO_2^{[FMQ]}$ values calculated in the conventional manner (Gudmundsson and Wood, 1995), to enable easier comparison with other similar studies of garnet peridotite xenoliths suites, which have all used the Gudmundsson and Wood (1995) calibration.

Several earlier studies have measured Fe^{3+} in garnet from kimberlite-bourne garnet peridotites from various cratons (Kaapvaal, Slave, Fennoscandian Shield) using either Mössbauer spectroscopy (Lazarov et al., 2009; McCammon and Kopylova, 2004; McCammon et al., 2001; Woodland and Koch, 2003; Woodland and Peltonen, 1999) or the electron microprobe based flank method (Creighton et al., 2009; Creighton et al., 2010; Höfer and Brey, 2007). An association between metasomatic enrichment in the cratonic lithosphere and oxidation has also been noted in these earlier studies. To our knowledge, this is the first demonstration of this effect in the Siberian Craton. In the Kaapvaal Craton, there is a steady decrease in $\Delta\log fO_2^{[FMQ]}$ with depth from values around 0 to −1 at ≈70 km depth to around −3.5 at ≈140 km depth (Woodland and Koch, 2003). At deeper levels, the rate of decrease of $\Delta\log fO_2^{[FMQ]}$ decreases, such that values at ≈220 km depth were around −4.2. Similar results were obtained by Lazarov et al. (Lazarov et al., 2009) for samples from the Finsch mine in the Kaapvaal Craton. In this case, $\Delta\log fO_2^{[FMQ]}$ decreased from −2.5 to −4.7 with increasing pressure from pressures of 4.4 to 6.5 GPa. However in the Finsch samples, there was no discernable break in slope of the $\Delta\log fO_2^{[FMQ]}-P$ profile at high pressures. Woodland and Koch (2003) attributed the overall decrease in mantle $\Delta\log fO_2^{[FMQ]}$ with increasing pressure to the positive molar volume change of the buffering reaction in garnet peridotite assemblages (reaction (1)) (Frost and McCammon, 2008). The Woodland and Koch (2003) samples from >140 km, where the slope of the $\Delta\log fO_2^{[FMQ]}-$depth trend decreased, were often those exhibiting textural evidence of shearing and generally more fertile compositions. All samples from ≥60 km depth derived from the diamond/graphite stability field (as opposed to carbonate stability) in depth-fO_2 space.

The mildly to extensively metasomatised garnet peridotite xenoliths from Kimberley in the Kaapvaal Craton showed sufficient levels of oxidation in some samples (up to $\Delta\log fO_2^{[FMQ]}=0$) to induce magnesite rather than diamond stability (Creighton et al., 2009). This effect was sufficiently strong to mask any depth-fO_2 relationship of the sort reported by Woodland and Koch (2003). A similar effect was reported in an investigation of garnet peridotite xenoliths from the Diavik kimberlite in the Slave Craton by Creighton et al. (2010). Samples from the Wessleton kimberlite (Griffin et al., 1999; McCammon et al., 2001) exhibit zoned garnet grains in which Ca-enriched rims crystallized on Ca-poor cores during a metasomatic event. The rims were shown, using the milli-Mössbauer technique, to be richer in Fe^{3+} than the cores, suggesting that metasomatism was associated with oxidation. During the metasomatic event, $\Delta\log fO_2^{[FMQ]}$ increased by up to about 1 log unit, from garnet core to rim, such that the rims approached the carbonate-limiting EMOD/G reaction (2).

The very reduced oxygen fugacities recorded by the deepest (≈5–7 GPa) of the depleted samples in the Udachnaya suite, and by many deeply-derived samples from other suites, probably preclude the existence of carbonatite melts as metasomatic agents, but are consistent with fluids dominated by CH_4+H_2O (Woodland and Koch, 2003) in equilibrium with diamond (i.e. fluids on the C-saturation surface — Taylor and Green, 1987). Such CH_4-rich fluids percolating upwards from the asthenosphere or the deepest cratonic lithosphere are expected to encounter progressively more oxidizing conditions at decreasing pressures, and may evolve towards the H_2O-maximum (Taylor and Green, 1987; Woodland and Koch, 2003) by oxidation of CH_4 to diamond. The associated increase in fluid water activity (a_{H2O}) may lead to redox melting at deep levels of the lithosphere (Foley, 2011; Taylor and Green, 1988), because of the well-known effect of minor quantities of H_2O-rich fluid in lowering peridotite-CH_4 solidii (Taylor and Green, 1988). However, this would probably require higher temperatures (<1400 °C) than recorded by the sheared xenolith suite at the time of their sampling by the host kimberlite (Fig. 7), as the H_2O-saturated peridotite solidus at 5–7 GPa is around 100–200 °C higher in temperature over this pressure interval (Green et al. 2010). During partial melting of garnet peridotite, Fe^{3+} is expected to behave incompatibly with a melt/residue partition coefficient of ≈0.1 (Canil and ONeill, 1996; Canil et al., 1994), mainly because modal abundances of Fe^{3+}-hosting phases (garnet and pyroxenes) will decrease in the more refractory residues after partial melting. Conversely, partial melts in equilibrium with the residue are expected to be relatively enriched in Fe^{3+}. If these partial melts segregate and move into nearby zones in which a_{H2O} or temperature is lower, they may metasomatise adjacent parts of the lithosphere by freezing and crystallizing garnet and clinopyroxene which is relatively Fe^{3+}-rich compared with the pre-metasomatic phases. This metasomatised material will hence record an increase in fO_2. A record of such a process may be preserved in rare garnet peridotite xenoliths such as those from the Wesselton kimberlite in the Kaapvaal Craton, with Ca-enriched metasomatic garnet rims overgrowing more refractory cores (Griffin et al., 1999). Mössbauer milli-probe measurements conducted on the rims and cores of these garnets demonstrated an increase in fO_2 in the rims relative to the cores, suggesting that oxidation was associated with metasomatism (McCammon et al., 2001). Preservation of

the rims on garnet implied that metasomatism occurred a very short time (<1 Ma) before transport of the xenoliths in the host kimberlite and near-surface quenching. However, if metasomatism had occurred a significantly greater time before removal of the xenoliths from the lithosphere, it is expected that diffusive re-equilibration and recrystallisation would have rehomogenised the sample, but the final $Fe^{3+}/\sum Fe$ content of the homogenized garnet would have remained higher than that of the pre-metasomatic garnet, thus recording increased fO_2. The enriched (metasomatised) Siberian samples are oxidized relative to the depleted samples and may have undergone a process similar to this.

6. Conclusions

(1) The Udachnaya East kimberlite has sampled garnet peridotite xenoliths from the underlying cratonic lithosphere from a depth range corresponding to pressures of 1.2 to 7.1 GPa. With one exception, samples derived from <5.2 GPa lie approximately on a typical cratonic geotherm of 40 mW m^{-2}. More deeply derived samples record temperatures ≥100 °C above this.

(2) The high temperature – high pressure samples mostly have sheared textures and evidence in garnet and clinopyroxene chemistry of enrichment, relative to the low temperature – low pressure group which exhibits mostly granular textures and depleted garnet and clinopyroxene chemistry. Thus, the Siberian cratonic lithosphere under the Undachnaya pipe consists of a relatively cool and depleted upper layer about 150 km deep, underlain by a hotter, sheared layer which extends to at least 210 km and contains both depleted and enriched material.

(3) The newly developed Fe K-edge XANES technique (Berry et al., 2010) was applied to garnets from this suite to determine their $Fe^{3+}/\sum Fe$ values. This enabled determination of a redox profile through the lithospheric section represented by the xenolith suite. An overall trend to lower $\Delta \log fO_2^{[FMQ]}$ values with increasing pressure was observed with $\Delta \log fO_2^{[FMQ]}$ varying from −2.5 to nearly −6.0 over the sampled pressure interval. This relates to the molar volume change of fO_2-dependent equilibria between Fe^{2+}/Fe^{3+}-bearing silicate phases (e.g. Frost and McCammon, 2008).

(4) Superimposed on this trend is an oxidation trend to $\Delta \log fO_2^{[FMQ]}$ values 1–2 units higher than the main molar volume-related trend. The more oxidized xenoliths are almost exclusively confined to the pressure interval from which the sheared and metasomatically enriched samples were derived, indicating a very clear link between metasomatism and oxidation. The amount of oxidation was insufficient to de-stabilize diamond in the deep lithosphere, however.

(5) CHO-fluids present in the very deepest parts of the lithosphere would have been CH_4-rich at the fO_2 values indicated by the deepest, depleted and most reduced xenoliths ($\Delta \log fO_2^{[FMQ]} \approx -6$). A possible mechanism for the metasomatism relates to localized, low degree "redox melting". It is envisaged that upwardly percolating $CH_4 \pm H_2O$ fluids would encounter progressively more oxidizing peridotite wall-rock, and would eventually become oxidized, leading to diamond crystallization and an increase in water activity in the fluid. This could lead to local partial melting and enriched melts could migrate into cooler parts of the lithosphere and crystallize, thus metasomatically enriching parts of the lithosphere. Melts thus formed are expected to be relatively enriched in Fe^{3+} as it is moderately incompatible during partial melting. Therefore, lithospheric domains metasomatised by solidification of these melts would be relatively enriched in Fe^{3+} and garnets may therefore have higher $Fe^{3+}/\sum Fe$ values, thus recording relatively higher $\Delta \log fO_2^{[FMQ]}$ values.

(6) Fe K-edge XANES (Berry et al., 2010) offers a highly spatially resolved and rapid technique for determination of $Fe^{3+}/\sum Fe$ in mantle-derived garnets with accuracy and precision similar to those of Mössbauer spectroscopy.

Acknowledgments

We gratefully acknowledge the assistance of Karsten Goemann and Sandrin Feig (Central Science Laboratory, University of Tasmania) with the electron microprobe analyses and Charlotte Allen (ANU) with the LA-ICPMS analyses. Part of this research was undertaken on the XFM beamline at the Australian Synchrotron, Victoria, Australia, and we gratefully acknowledge the assistance of the beamline scientists, David Paterson, Martin de Jonge and Daryl Howard. Jesse Jones (ANU) also assisted with collection of the XANES spectra. The manuscript benefited from discussions with Gerhard Brey, Dmitri Ionov, Hugh O'Neill and Anja Rosenthal. An earlier version of the manuscript was improved by constructive formal reviews from John Foden and Steven Creighton. This work was partly funded by an Australian Research Council (ARC) Future Fellowship to GY and an ARC Professorial Fellowship and Discovery Grant to VK.

Appendix A. Supplementary data

Supplementary data to this article can be found online at doi:10.1016/j.lithos.2012.01.016.

References

Agashev, A.M., Pokhilenko, N.P., Cherepanova, Y.V., Golovin, A.V., 2010. Geochemical evolution of rocks at the base of the lithopspheric mantle: evidence from study of xenoliths of deformed peridotites from kimberlite of the Udachnaya Pipe. Doklady Earth Sciences 432, 746–749.

Ashchepkov, I.V., Pokhilenko, N.P., Vladykin, N.V., Logvinova, A.M., Afanasiev, V.P., Pokhilenko, L.N., Kuligin, S.S., Malygina, E.V., Alymova, N.A., Kostrovitsky, S.I., Rotman, A.Y., Mityukhin, S.I., Karpenko, M.A., Stegnitsky, Y.B., Khemelnikova, O.S., 2010. Structure and evolution of the lithospheric mantle beneath Siberian craton, thermobarometric study. Tectonophysics 485, 17–41.

Belonoshko, A.B., Saxena, S.K., 1992. A unified equation of state for fluids of C–H–O–N–S–Ar composition and their mixtures up to very high temperatures and pressures. Geochimica et Cosmochimica Acta 56, 3611–3626.

Berry, A.J., Danyushevsky, L.V., O'Neill, H.St.C., Newville, M., Sutton, S.R., 2008. Oxidation state of iron in komatiitic melt inclusions indicates hot Archaean mantle. Nature 455, 960–963.

Berry, A.J., Yaxley, G.M., Woodland, A.B., Foran, G.J., 2010. A XANES calibration for determining the oxidation state of iron in mantle garnet. Chemical Geology 278, 31–37.

Boyd, F.R., Pokhilenko, N.P., Pearson, D.G., Mertzman, S.A., Sobolev, N.V., Finger, L.W., 1997. Composition of the Siberian cratonic mantle: evidence from Udachnaya peridotite xenoliths. Contributions to Mineralogy and Petrology 128, 228–246.

Brey, G.P., Kohler, T., 1990. Geothermobarometry in 4-Phase Lherzolites. 2. New thermobarometers, and practical assessment of existing thermobarometers. Journal of Petrology 31, 1353–1378.

Canil, D., ONeill, H.S.C., 1996. Distribution of ferric iron in some upper-mantle assemblages. Journal of Petrology 37, 609–635.

Canil, D., Oneill, H.S., Pearson, D.G., Rudnick, R.L., Mcdonough, W.F., Carswell, D.A., 1994. Ferric iron in peridotites and mantle oxidation-states. Earth and Planetary Science Letters 123, 205–220.

Creighton, S., Stachel, T., Matveev, S., Hofer, H., McCammon, C., Luth, R.W., 2009. Oxidation of the Kaapvaal lithospheric mantle driven by metasomatism. Contributions to Mineralogy and Petrology 157, 491–504.

Creighton, S., Stachel, T., Eichenberg, D., Luth, R., 2010. Oxidation state of the lithospheric mantle beneath Diavik diamond mine, central Slave craton, NWT, Canada. Contributions to Mineralogy and Petrology 159, 645–657.

Cross, J.O., Frenkel, A.I., 1999. Use of scattered radiation for absolute X-ray energy calibration. Review of Scientific Instruments 70, 38–40.

Eggins, S.M., Rudnick, R.L., McDonough, W.F., 1998. The composition of peridotites and their minerals: a laser-ablation ICP-MS study. Earth and Planetary Science Letters 154, 53–71.

Eggler, D.H., Baker, D.R., 1982. Reduced volatiles in the system C–O–H: implications to mantle melting, fluid formation and diamond genesis. In: Akimoto, S., Manghnani, M.H. (Eds.), High Pressure Research in Geophysics. Center for Academic Publications Japan, Tokyo, pp. 237–250.

Foley, S.F., 2011. A reappraisal of redox melting in the earth's mantle as a function of tectonic setting and time. Journal of Petrology 52, 1363–1391.

Frost, B.R., 1991. Oxide minerals: petrologic and magnetic significance. In: Lindsley, D.H. (Ed.), Reviews in Mineralogy. Mineralogical Society of America.

Frost, D.J., McCammon, C.A., 2008. The redox state of Earth's mantle. Annual Review of Earth and Planetary Science 36, 389–420.

Green, D.H., Hibberson, W.O., Kovács, I., Rosenthal, A., 2010. Water and its influence on the lithosphere-asthenosphere boundary. Nature 467, 448–452.
Griffin, W.L., Ryan, C.G., 1995. Trace-elements in indicator minerals — area selection and target evaluation in diamond exploration. Journal of Geochemical Exploration 53, 311–337.
Griffin, W.L., Shee, S.R., Ryan, C.G., Win, T.T., Wyatt, B.A., 1999. Harzburgite to lherzolite and back again: metasomatic processes in ultramafic xenoliths from the Wesselton kimberlite, Kimberley, South Africa. Contributions to Mineralogy and Petrology 134, 232–250.
Grütter, H.S., Gurney, J.J., Menzies, A.H., Winter, F., 2004. An updated classification scheme for mantle-derived garnet, for use by diamond explorers. Lithos 77, 841–857.
Gudmundsson, G., Wood, B.J., 1995. Experimental tests of garnet peridotite oxygen barometry. Contributions to Mineralogy and Petrology 119, 56–67.
Höfer, H.E., Brey, G.P., 2007. The iron oxidation state of garnet by electron microprobe: its determination with the flank method combined with major-lement analysis. American Mineralogist 92, 873–885.
Ionov, D.A., Doucet, L.S., Ashchepkov, I.V., 2010. Composition of the lithospheric mantle in the Siberian Craton: new constraints from fresh peridotites in the Udachnaya-East Kimberlite. Journal of Petrology 51, 2177–2210.
Kamenetsky, V.S., Kamenetsky, M.B., Sobolev, A.V., Golovin, A.V., Sharygin, V.V., Pokhilenko, N.P., Sobolev, N.V., 2009. Can pyroxenes be liquidus minerals in the kimberlite magma. Lithos 112S, 213–222.
Kinny, P.D., Griffin, B.J., Heaman, L.M., Brakhfogel, F.F., Spetsius, Z.V., 1997. SHRIMP U-Pb ages of perovskite from Yakutian kimberlites. Geologiya i Geofizika 38, 91–99.
Lazarov, M., Woodland, A.B., Brey, G.P., 2009. Thermal state and redox conditions of the Kaapvaal mantle: a study of xenoliths from the Finsch mine, South Africa. Lithos 112, 913–923.
Luth, R.W., 1993. Diamonds, eclogites, and the oxidation state of the Earth's mantle. Science 261, 66–68.
McCammon, C., Kopylova, M.G., 2004. A redox profile of the Slave mantle and oxygen fugacity control in the cratonic mantle. Contributions to Mineralogy and Petrology 148, 55–68.
McCammon, C.A., Griffin, W.L., Shee, S.R., O'Neill, H.S.C., 2001. Oxidation during metasomatism in ultramafic xenoliths from the Wesselton kimberlite, South Africa: implications for the survival of diamond. Contributions to Mineralogy and Petrology 141, 287–296.
Nickel, K.G., Green, D.H., 1985. Empirical geothermobarometry for garnet peridotites and implications for the nature of the lithosphere, kimberlites and diamonds. Earth and Planetary Science Letters 73, 158–170.
Nimis, P., Grütter, H., 2010. Internally consistent geothermometers for garnet peridotites and pyroxenites. Contributions to Mineralogy and Petrology 159, 411–427.
O'Neill, H. St C., Wall, V.J., 1987. The olivine-orthopyroxene-spinel oxygen geobarometer, the Ni precipitation curve and the oxygen fugacity of the Earth's upper mantle. Journal of Petrology 28, 1169–1191.
Paterson, D., de Jonge, M.D., Howard, D.L., Lewis, W., McKinlay, J., Starritt, A., Kusel, M., Ryan, C.G., Kirkham, R., Moorhead, G., Siddons, D.P., 2011. The X-ray fluorescence microscopy beamline at the Australian synchrotron. American Institute of Physics Conference Proceedings 1365, 219–222.
Pokhilenko, N.P., Sobolev, N.V., Kuligin, S.S., Shimuzu, N., 1999. Peculiarities of distribution of pyroxenite paragenesis garnets in Yakutian kimberlites and some aspects of the evolution of the Siberian cratonic lithospheric mantle. Proceedings of the 7th International Kimberlite Conference, pp. 689–698.
Pollack, H.N., Chapman, D.S., 1977. On the regional variation of heat flow, geotherms, and lithospheric thickness. Tectonophysics 38, 279–296.
Shimizu, N., Pokhilenko, N.P., Boyd, F.R., Pearson, D.G., 1997. Geochemical characteristics of mantle xenoliths from Udachnaya kimberlite pipe. Geologiya i Geofizika 38, 194–205.
Sobolev, N.V., Logvinova, A.M., Zedgenizov, D.A., Pokhilenko, N.P., Malygina, E.V., Kuzmin, D.V., Sobolev, A.V., 2009. Petrogenetic significance of minor elements in olivines from diamonds and peridotite xenoliths from kimberlites of Yakutia. Lithos 112 (S2), 701–713.
Stachel, T., Viljoen, K.S., Brey, G., Harris, J.W., 1998. Metasomatic processes in lherzolitic and harzburgitic domains of diamondiferous lithospheric mantle: REE in garnets from xenoliths and inclusions in diamonds. Earth and Planetary Science Letters 159, 1–12.
Stachel, T., Aulbach, S., Brey, G.P., Harris, J.W., Leost, I., Tappert, R., Viljoen, K.S., 2004. The trace element composition of silicate inclusions in diamonds: a review. Lithos 77, 1–19.
Sun, S.-S., McDonough, W.F., 1989. Chemical and isotopic systematics of oceanic basalts: implications for mantle compositions and processes. In: Saunders, A.D., Norry, M.J. (Eds.), Magmatism in the Ocean Basins. Geological Society Special Publication, pp. 313–345.
Taylor, W.R., 1998. An experimental test of some geothermometer and geobarometer formulations for upper mantle peridotites with application to the thermobarometry of fertile lherzolite and garnet websterite. Neues Jahrbuch Mineralogie Abhandlung 172, 381–408.
Taylor, W.R., Green, D.H., 1987. The petrogenic role of methane: effect on liquidus phase relations and the solubility mechanism of reduced C-H volatiles. The Geochemical Society Special Publication No. 1, pp. 121–137.
Taylor, W.R., Green, D.H., 1988. Measurement of reduced peridotite–C–O–H solidus and implications for redox melting of the mantle. Nature 332, 349–352.
Woodland, A.B., Koch, M., 2003. Variation in oxygen fugacity with depth in the upper mantle beneath the Kaapvaal craton, Southern Africa. Earth and Planetary Science Letters 214, 295–310.
Woodland, A.B., Peltonen, P., 1999. Ferric iron contents of garnet and clinopyroxene and estimated oxygen fugacities of peridotite xenoliths from the Eastern Finland Kimberlite Province. Proc. 7th Int. Kimberlite Conf., 7th. Red Roof Design, Cape Town, pp. 904–911.
Woodland, A.B., Ross II, C.R., 1994. A crystallographic and Mössbauer spectroscopic study of $Fe_3Al_2Si_3O_{12}$–$Fe^{2+}{}_3Fe^{3+}{}_2Si_3O_{12}$ (almandine–skiaigite) and $Ca_3Fe^{3+}{}_2Si_3O_{12}$–$Fe^{2+}{}_3Fe^{3+}{}_2Si_3O_{12}$ (andradite–skiagite) garnet solid solutions. Physics and Chemistry of Minerals 21, 117–132.
Woodland, A.B., Angel, R.J., Koch, M., Kunz, M., Miletich, R., 1999. Eqautions of state for $Fe^{2+}{}_3Fe^{3+}{}_2Si_3O_{12}$ "skiagite" garnet and Fe_2SiO_4–Fe_3O_4 spinel solid solutions. Journal of Geophyscial Research 104 (B9), 20,049–20,058.
Woodland, A.B., Bauer, M., Boffa Ballaran, T., Hanrahan, M., 2009. Crystal chemistry of $Fe^{2+}{}_3Cr_2Si_3O_{12}$–$Fe^{2+}{}_3Fe^{3+}{}_2Si_3O_{12}$ garnet solid solutions and related spinels. American Mineralogist 94, 359–366.